Quantifying the Near-Future Wind Energy Production over the North Sea Using a Novel Statistical–Dynamical Approach to GCM Downscaling

RUBEN BORGERS,[a] JOAQUIM G. PINTO,[b] AND NICOLE VAN LIPZIG[a]

[a] *Department of Earth and Environmental Sciences, KU Leuven, Leuven, Belgium*
[b] *Institute of Meteorology and Climate Research Troposphere Research (IMKTRO), Karlsruhe Institute of Technology, Karlsruhe, Germany*

(Manuscript received 27 June 2024, in final form 12 December 2024, accepted 24 January 2025)

ABSTRACT: The increasing importance of wind energy in the electricity mix underscores the need for accurate estimation of wind energy production in the coming decades. Here, we present a new statistical–dynamical downscaling approach to quantify the energy production of wind farms in an ensemble of future climate projections. This approach relies on two reanalysis-driven regional climate model simulations, one of which includes a wind farm parameterization to account for wind farm–atmosphere interactions and wake losses. We then apply this method to a projected, 92-GW offshore wind farm distribution in the North Sea and compare the energy production between the wind climate of 1985–2014 and 38 projections for the wind climate of 2025–54. The ensemble mean difference in 30-yr energy production is −5% for JJA, −2.5% for SON, and near zero for DJF and MAM. However, these 30-yr differences have a large ensemble spread, with an interquartile range (IQR) of around 8% and a range of around 15%. Furthermore, the ensemble probability distribution of decadal energy production is different compared to the reference period. For winter, 16% of future decades fall below the 5th percentile (P5) of the historical period and 12% of future decades exceed the 95th percentile (P95). Finally, we demonstrate the importance of considering the secondary effect by which wind climate changes increase or reduce wake losses, as long-term changes can differ strongly when these effects are not included. The potential changes in energy production discussed here should be considered alongside other effects, such as near-future increases in interfarm wake losses and technological advancements to optimally constrain the uncertainty in near-future wind energy production.

SIGNIFICANCE STATEMENT: Wind energy is playing an increasingly significant role in the electricity mix, making it essential to quantify the uncertainty in near-future wind energy production for developing secure energy infrastructure. In this context, we introduce a novel approach that combines future climate projections with high-resolution regional climate model simulations to quantify the uncertainty in future energy production in a cost-effective way. Improving upon existing methods, this approach also considers the two-way interactions between wind farm clusters and the atmosphere.

KEYWORDS: Wind; Downscaling; Renewable energy; Mesoscale models; Climate; General circulation models

1. Introduction

As part of the urgent transition to low-carbon energy systems, the offshore wind energy sector reached a global capacity of 72.6 GW at the end of 2023 compared to 7.1 GW at the end of 2013 (International Renewable Energy Agency 2024). In Europe, the offshore capacity is planned to increase to between 300 and 450 GW by 2050 in order to achieve climate neutrality (European Commission 2020). How much energy a wind farm will actually produce over its lifetime depends on the available wind resource, which is usually quantified in a preconstruction wind resource assessment. Such assessments are typically based on (a combination of) historical measurements and reanalysis data (e.g., Kim et al. 2022; Zekeik et al. 2024), with the implicit assumption of climate stationarity. However, the future wind resource might differ from a historical reference period as a consequence of long-term climate variability and climate change (Feser et al. 2015; Bodini et al. 2016; Karnauskas et al. 2018). Previous studies addressing the uncertainty in future wind resources and energy production have relied on global climate model (GCM) projections from the Coupled Model Intercomparison Project (CMIP), which cover a range of greenhouse gas emission scenarios embedded in different shared socioeconomic pathways (SSPs).

A common approach is to directly analyze the GCM data (e.g., Fant et al. 2016; Devis et al. 2018; Zhao et al. 2024), but the resolution of these data is usually low (grid spacing ≥ 100 km) so this approach is only suitable for regional or global analyses. Various methods have been developed to downscale wind fields and enhance the GCM projections to higher spatial and temporal resolution (Pryor and Hahmann 2019). One approach is the dynamical downscaling of GCM projections with higher-resolution regional climate models (RCMs), which has been used extensively to quantify future wind resources (e.g., Hueging et al. 2013). Because the downscaling of GCM simulations has a very high computational cost,

---

Supplemental information related to this paper is available at the Journals Online website: https://doi.org/10.1175/JAMC-D-24-0116.s1.

Corresponding author: Ruben Borgers, ruben.borgers@kuleuven.be

DOI: 10.1175/JAMC-D-24-0116.1

hybrid statistical–dynamical methods have also been employed where selected cases are dynamically downscaled and extrapolated statistically to longer periods (e.g., Mengelkamp 1999; Najac et al. 2011; Reyers et al. 2015). The three aforementioned approaches have been applied to study the future wind resources over the European North Sea: Carvalho et al. (2021) found a decrease of wind resources for 2045–65 based on the analysis of 15 CMIP6 GCMs, with stronger reductions under SSP5-8.5 than under SSP2-4.5 and stronger reductions for summer than for winter. Hahmann et al. (2022) only found a decreased wind resource over summer for 2031–50 based on the analysis of 16 CMIP6 GCMs under SSP5-8.5. In both these studies, the findings were characterized by a large ensemble spread. Research based on (statistical)dynamical downscaling has mostly been restricted to CMIP5 driving GCMs and downscaled products with a grid spacing ≥ 12 km. Moemken et al. (2018) analyzed an ensemble of four GCMs downscaled by two RCMs and did not find a change in the mean wind resource over the North Sea for 2031–50. However, they did find a decrease in the summer wind resource for the period 2071–2100. Comparability between different studies is limited due to the use of different ensembles in terms of size, models, scenarios, and periods.

Because wind resource changes derived from CMIP5 and CMIP6 have been shown to differ substantially (Carvalho et al. 2021; Jung and Schindler 2022), there is a need for downscaled versions of the next-generation CMIP6 model simulations. However, several factors limit the applicability of existing downscaling methods in quantifying future energy production uncertainty at the level of a wind farm. First, the wind resource changes are usually not dynamically linked to the actual energy production of a wind farm. Offshore wind turbines and wind farms are so large that they interact with the large-scale flow, which can substantially impact the efficiency through waking inside and between wind farms (e.g., Volker et al. 2017; Fischereit et al. 2022b; Borgers et al. 2024). The sensitivity of a wind farm to these wake effects also depends on the local wind climate, so that future wind climate changes can either reduce or increase the impact of these processes. To include these wind farm–atmosphere interactions, kilometer-scale RCM simulations are needed that can include a parameterization of these interactions. Full dynamical downscaling of a large ensemble of CMIP6 simulations is unfeasible at this grid resolution, so a new statistical–dynamical approach is required which uses kilometer-scale RCM simulations. Furthermore, the existing statistical–dynamical approaches often use a wind speed class resolution that is too coarse given the highly nonlinear relationship between wind speed and wind turbine power production. Moreover, only a limited number of cases are typically calculated for each class, so that the underlying atmospheric variability might not be fully captured. Finally, the statistical part of these algorithms is generally applied to higher-level winds (e.g., 850 hPa) instead of turbine-level winds, which can lead to errors due to a lack of vertical correlation and/or the use of vertical extrapolations during postprocessing.

In this study, we propose a new statistical–dynamical downscaling algorithm to estimate the future wind energy production and its uncertainty for one or several wind farms. This algorithm uses high-resolution RCM simulations driven by reanalysis data and includes a mesoscale wind farm parameterization in the RCM to account for wind farm–atmosphere interactions. These simulations provide a lookup table where wind farm energy production is given as a function of wind speed and direction, which can be used to calculate energy production in the future wind climate of a GCM. We apply the algorithm to an ensemble of 38 future GCM simulations to quantify the near-future energy production of a projected, 92-GW wind farm distribution in the North Sea. Section 2 describes the different datasets and model simulations used in this study, in addition to the statistical–dynamical downscaling algorithm. Section 3 presents the results of the GCM analysis and of the downscaling algorithm, followed by a discussion of the method and results in section 4. Finally, conclusions are formulated in section 5.

2. Data and methods

a. *Processing of GCM data*

The GCM simulation output used in this work was generated within phase 6 of the CMIP (CMIP6) (Eyring et al. 2016). This output was downloaded from the Earth System Grid Federation (ESGF) data nodes (Petrie et al. 2021), using Wget scripts generated in the online search interface. Data were obtained for a historical reference period (1985–2014) and the near future (2025–54). The historical simulations are part of the historical experiment of the CMIP activity, while the future data are part of the SSP experiment of the Scenario Model Intercomparison Project (ScenarioMIP) activity. Table 1 gives an overview of the 17 GCMs considered in this study. For each GCM, a simulation for each fully available SSP scenario was included. Many CMIP6 models could not be included in this work: In some cases, the necessary data at model levels were not available. For other models, downloads did not start or failed repeatedly for large file sizes. Two models were not included based on the poor performance found for these models by Hahmann et al. (2022) in terms of simulating the North Sea wind climate at turbine level. The choice to consider 30-yr periods is based on several reasons. First of all, it is comparable to the lifespan of the turbines in an offshore wind farm (Li et al. 2022). Second, the World Meteorological Organization (WMO) recommends at least three consecutive 10-yr periods for calculating climate normals (World Meteorological Organization 2017). Third, wind resource assessments at offshore wind farm development sites have generally not considered periods longer than 30 years (Sempreviva et al. 2008; Carta et al. 2013).

The calculation of wind speed and wind direction at typical wind turbine nacelle heights (∼100 m) was performed analogously to the method detailed in Hahmann et al. (2022). The necessary variables were downloaded from the 6hrLev table, i.e., instantaneous data at model levels at 6-hourly intervals. For models with a pressure-based vertical coordinate, also temperature (ta), surface pressure (ps), and specific humidity (hus) were required to compute the height of the model levels at each time step by vertically integrating the hypsometric equation. For the vertical interpolation of wind speed, the

TABLE 1. Overview of the considered CMIP6 models and simulations. Models for which the experiment matrix is filled with — were excluded based on the historical performance analysis.

Model	Atmospheric component	Grid spacing (lon × lat)	ScenarioMIP experiment[a]							Variant[b]	Reference
			1-1.9	1-2.6	2-4.5	3-7.0	4-3.4	4-6.0	5-8.5		
ACCESS-CM2	HadGAM/UM	1.25° × 1.875°		x	x	x			x	r5i1p1f1	Bi et al. (2020)
CanESM5	CanAM	2.8125° × 2.79°	—	—	—	—	—	—	—	r1i1p2f1	Swart et al. (2019)
CMCC-CM2-SR5	CAM	1.25° × 0.94°	—	—	—	—	—	—	—	r1i1p1f1	Cherchi et al. (2019)
CNRM-CM6-1	ARPEGE	1.4° × 1.4°		x					x	r1i1p1f2	Voldoire et al. (2019)
CNRM-ESM2-1	ARPEGE	1.4° × 1.4°	x	x	x	x			x	r1i1p1f2	Séférian et al. (2019)
FGOALS-g3	GAMIL	2° × 2.25°		x		x	x			r1i1p1f1	Li et al. (2020)
GISS-E2-1-G	ModelE	2.5° × 2°			x				x	r1i1p1f2	Kelley et al. (2020)
HadGEM3-GC31-MM	HadGAM/UM	0.833° × 0.556°		x					x	r1i1p1f3	Sellar et al. (2020)
IPSL-CM5A2-INCA	LMDZ	3.75° × 1.875°	—	—	—	—	—	—	—	r1i1p1f1	Sepulchre et al. (2020)
IPSL-CM6A-LR	LMDZ	2.5° × 1.27°	x	x	x	x		x	x	r1i1p1f1	Boucher et al. (2020)
MPI-ESM1-2-HR	ECHAM	0.9375° × 0.935°		x	x	x			x	r1i1p1f1	Müller et al. (2018)
MPI-ESM1-2-LR	ECHAM	1.875° × 1.865°		x		x				r1i1p1f1	Mauritsen et al. (2019)
MRI-ESM2-0	GSMUV	1.125° × 1.121°		x					x	r1i1p1f1	Kawai et al. (2019)
NorESM2-LM	CAM	2.5° × 1.895°	—	—	—	—	—	—	—	r1i1p1f1	Seland et al. (2020)
NorESM2-MM	CAM	1.25° × 0.94°			x	x				r1i1p1f1	Seland et al. (2020)
TaiESM1	CAM	1.25° × 1.0.94°	—	—	—	—	—	—	—	r1i1p1f1	Lee et al. (2020)
UKESM1-0-LL	HadGAM/UM	1.25° × 1.875°		x	x	x			x	r1i1p1f2	Sellar et al. (2020)

[a] Each ScenarioMIP experiment is based on a global socioeconomic scenario and an associated end-of-century (2100) radiative forcing. For example, SSP3-7.0 consists of a socioeconomic scenario SSP3 ("A Rocky Road") and a radiative forcing of 7 $\mathrm{Wm^{-2}}$ by 2100 compared to the preindustrial baseline (O'Neill et al. 2016).

[b] The ripf code identifies each individual simulation performed by a model for a given experiment in terms of the realization (r), initialization method (i), model physics (p), and forcing specification (f).

power law was used in which the power (shear) coefficient was inferred from the model levels above and below the target height as in Borgers et al. (2024). For wind direction, the zonal and meridional wind components were first linearly interpolated to the target height.

The different GCMs were evaluated in terms of their ability to represent the historical wind climate over the study area. With this aim, seasonal wind roses of each GCM were compared at a central location in the North Sea (55°N, 3°E) with their counterparts in the ERA5 reanalysis (Hersbach et al. 2020). ERA5 has been shown to agree well with offshore wind measurements (e.g., Hahmann et al. 2022; Kalverla et al. 2020) and to outperform other reanalyses for the characterization of offshore wind resources (Olauson 2018; Soares et al. 2020). The seasonal wind roses were compared with the Perkins skill score (PSS), which expresses the fraction of overlap between two histograms:

$$\mathrm{PSS}(W_1, W_2) = \sum_{i=1}^{n} \sum_{j=1}^{m} \mathrm{MIN}(F_{W_1}^{ij}, F_{W_2}^{ij}), \tag{1}$$

where W is a wind rose, i.e., a two-dimensional histogram of wind speed and wind direction; n (m) is the number of wind speed (direction) bins; and F represents the normalized frequency in a wind rose bin. The PSS ranges between 0 and 1, where 1 represents the complete overlap. Prior to the comparison, the ERA5 winds were first regridded to the GCM scale. Whereas most of the work presented here uses the GCM winds interpolated from model levels, a first assessment of wind climate differences between the historical and future periods was carried out based on surface winds, also at a temporal resolution of 6 h. This assessment was done during the downloading and processing of the model-level datasets. For all applications of the GCM data, except for the performance analysis, the historical and future wind speed data were first bias corrected using a per-season quantile mapping approach (e.g., Li et al. 2019), with ERA5 as the reference.

b. *COSMO-CLM configuration*

The regional simulations were performed with the regional climate model COSMO-CLM (version 5.0-15), codeveloped between the Consortium for Small-Scale Modeling (COSMO) and the Climate Limited-Area Modeling Community (CLM-Community) (Rockel et al. 2008). The primitive equations are formulated in nonhydrostatic, compressible form and are integrated with a Runge–Kutta dynamical core (Doms and Baldauf 2013). The model grid is made up of a rotated longitude–latitude grid with a height-based, terrain-following coordinate. The model setup used in this study is mostly identical to the one of Borgers et al. (2024). The horizontal domain covers most of the North Sea using a grid increment of 0.025° (~2.8 km), corresponding to 339 and 409 grid cells in the zonal and meridional directions, respectively (Fig. 1). The lateral boundary forcing was applied within the 40-km-wide relaxation zone and was derived from the ERA5 reanalysis at hourly frequency. No intermediate nesting stages were used, following sensitivity experiments from Brisson et al. (2016) and Borgers et al. (2024). The vertical dimension of the grid consists of 61 vertical levels with a spacing of approximately 30 m at turbine rotor height. Interactions between the atmosphere and Earth's surface are accounted for by roughness- and stability-dependent surface flux parameterizations, in addition to the multilayer soil model TERRA-ML (Doms et al. 2013). In the

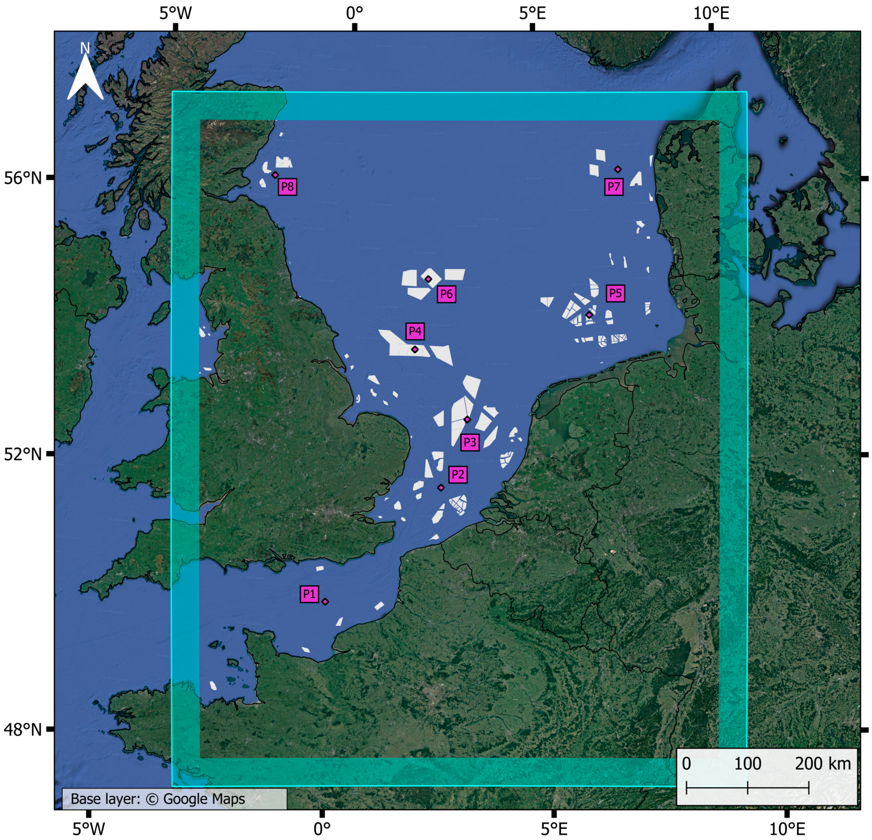

FIG. 1. Map showing the relaxation boundaries of the model domain (cyan), the projected wind farm distribution for 2030 (white polygons), and the eight locations where the weighting algorithm was applied (purple points).

planetary boundary layer (PBL), subgridscale turbulent fluxes are parameterized using a one-dimensional, turbulent kinetic energy (TKE)-based diagnostic closure scheme after Mellor and Yamada (1982). Furthermore, the feedback of gridscale cumulus convection on the model variables is represented by the bulk cloud parameterization of Tiedtke (1989). Finally, radiative processes are taken into account with the radiative transfer scheme of Ritter and Geleyn (1992). An extensive description of the model system is available in the documentation (e.g., Doms and Baldauf 2013). The skill of COSMO-CLM in modeling the North Sea wind climate has been thoroughly compared to data from 19 in situ measurement stations, five wind lidars, and Advanced Scatterometer (ASCAT) satellite measurements (Borgers et al. 2024). In general, the wind climate at turbine rotor height is modeled well and captures the observed directional, seasonal, and interannual variability.

To represent the wind farm–atmosphere interactions, the Fitch wind farm parameterization (WFP) (Fitch et al. 2012) was included. This additional module represents the wind farm forcing on the atmosphere as a sink of kinetic energy and a source of TKE, which is applied over the vertical layers that intersect the turbine rotor. The original implementation in COSMO5-CLM15 (Chatterjee et al. 2016; Akhtar and Chatterjee 2020) has previously been updated with several improvements as described in Borgers et al. (2024). For the simulations in this study, the code was further updated to allow rotor height and diameter, turbine density and turbine power, and thrust curves C_p and C_t to vary spatially. Also, other schemes exist to represent this wind farm forcing and the different schemes can lead to significant differences (Fischereit et al. 2022a; Ali et al. 2023). However, the Fitch WFP has been shown to perform well in modeling wind speed deficits behind wind farms compared to observational datasets in HARMONIE–AROME (van Stratum et al. 2022; Dirksen et al. 2022), the Weather Research and Forecasting (WRF) Model (Garcia-Santiago et al. 2022), and COSMO-CLM (Akhtar et al. 2021). In addition, studies have found that modeled wind speed reductions inside wind farms also agree well with airborne and in situ measurements (Ali et al. 2023; Dirksen et al. 2022) and Reynolds-averaged Navier–Stokes (RANS) simulations (Fischereit et al. 2022c).

Two simulations were performed for the period 1990–2020. One simulation did not incorporate any wind farms and is used to represent the undisturbed wind climate. The other simulation included a projected wind farm distribution for 2030, which will be described in detail in the next subsection. The entire first year was used for temporal spinup of the soil layers and is omitted from the analysis based on Jerez et al. (2020). A simulation length of 30 years was chosen for reasons described in section 2a.

c. The wind farm distribution

The methodology described in this study was tested for a time-invariant, projected wind farm distribution for 2030, with a total capacity of 92 GW (Fig. 1). Whereas this time horizon does not correspond to the center of the time period considered for the future GCM simulations, i.e., 2025–54, it already represents a 30% completion of the target for 2050 according to the Ostend Declaration (2023). In addition, it is more clearly established which wind farm zones should be occupied by the year 2030, including the characteristics of those wind farms, such as turbine type and turbine spacing. After this time horizon, both the locations and characteristics of future wind farms are highly uncertain. Based on the projected wind farm distributions used in other studies (e.g., Rosencrans et al. 2024; Borgers et al. 2024), it was expected that wind farm–atmosphere interactions would be important for this 92-GW distribution.

The inputs for the wind farm parameterization are the spatial extent of each wind farm, the turbine specifications (hub height, rotor diameter, C_p curve, and C_t curve), and the turbine density. The basis of the developed wind farm distribution is the set of wind farms that were operational at the beginning of 2023. The spatial extent and total capacity of these wind farms were obtained from the European Marine Observation and Data Network (EMODnet) (EMODnet 2023). The turbine dimensions and rating were retrieved from the websites of the different wind farm projects. The turbine density was then calculated from the spatial extent, total capacity, and turbine rating at each wind farm. Since the thrust and power curves of the turbines are usually not publicly available, an approximation method was used. For this, 16 C_p–C_t couples were used from the study of van Stratum et al. (2022) in addition to those of three reference wind turbines (RWTs): the 5-MW RWT of the National Renewable Energy Laboratory (NREL) (Jonkman et al. 2009), the 10-MW RWT of the Technical University of Denmark (DTU) (Bak et al. 2013), and the 15-MW RWT of the International Energy Agency (IEA) (Gaertner et al. 2020). The operational wind farms that were also included in the simulations of van Stratum et al. (2022) were equipped with the power and thrust curves used in their work. For all other operational wind farms, the approximation method was applied. This method relies on the equation for the power generation of a wind turbine:

$$P = \frac{1}{2}\rho A C_p(V)V^3, \tag{2}$$

where P is the power output, ρ is a standard air density of 1.225 kg m^{-3}, A is the rotor area, V is the wind speed, and C_p is the wind speed-dependent power coefficient. This relationship $P(V)$ is highly nonlinear, with an increase in power output from the cut-in wind speed ($\sim$3 m s^{-1}) to the rated wind speed ($\sim$12 m s^{-1}), followed by constant power up to the cut-out wind speed ($\sim$25 m s^{-1}) above which the turbine blades are stalled to prevent damage (see Fig. S1 in the online supplemental material for an example). Based on the known rotor diameter at each operational wind farm, the C_p curve (and corresponding C_t curve) was selected for which the best match was found between the rated power derived from Eq. (2) and the known turbine rating. More specifically, the power production derived from Eq. (2) in the wind speed range of 17–20 m s^{-1} was compared to the publicly available turbine rating at each wind farm. The resulting difference in rated power could go from more than 50% for the worst match to well below 5% for the best match out of the 19 C_p curves (e.g., Figs. S1 and S2). The rationale behind this approach is that the ratio between the turbine rating and the turbine rotor diameter determines the shape of the power curve. To accommodate for the small mismatch coming from the approximation method, the turbine density in each wind farm was slightly reduced or increased to keep the total wind farm capacity unaffected.

TABLE 2. Description of the wind farm groups assigned to the points P1–P8. The areal density is computed by dividing the total wind farm surface area by the area of the smallest circle, centered around the point where the weighting algorithm is applied, which contains all of the wind farms assigned to that point.

Point	No. of wind farms	Total capacity (GW)	Mean capacity density (MW km^{-2})	Areal density (%)
P1	4	1.85	5.5	1.1
P2	32	12.3	10	6
P3	18	23.1	7.1	13
P4	10	9.8	4.5	8.6
P5	41	25.2	11.6	11.1
P6	4	5.1	2.2	20
P7	7	5.0	4.7	5.1
P8	5	2.9	4.7	4.3

The projected capacity per country is based on pledges formulated in the Ostend Declaration (2023). For wind farms expected to be operational by 2030, wind farm locations and planned capacities were mostly obtained from the EMODnet database. Some additional zones were retrieved from the Royal Belgian Institute for Natural Sciences (RBINS) for Belgium and France (Vigin 2022), from Rijkswaterstraat (2023) for the Netherlands, from the Crown Estate (2023) for the United Kingdom, from the work of Hahmann et al. (2022) for Denmark, and the work of Slavik et al. (2019) for Germany. For the planned wind farms where the turbine dimensions were already announced, only the C_p–C_t curves needed to be determined, which was done with the previously described approximation method. For the remaining planned wind farms, the 15-MW RWT was chosen, including the corresponding C_p and C_t curves, as 15-MW turbines are expected to be used for projects in the second half of this decade (Bento and Fontes 2019; Shields et al. 2021). The specifications of the wind farm groups linked to each of the eight points (see Fig. 1) are summarized in Table 2. The reasoning behind assigning the wind farms to different points will be detailed in the next section. Finally, the complete input layers for the wind farm parameterization are visualized in the supplements (see Fig. S3).

d. The weighting algorithm

The weighting algorithm was developed to estimate the energy production (EP) of one or several clustered wind farms under the wind climate simulated by a GCM. It relies on two

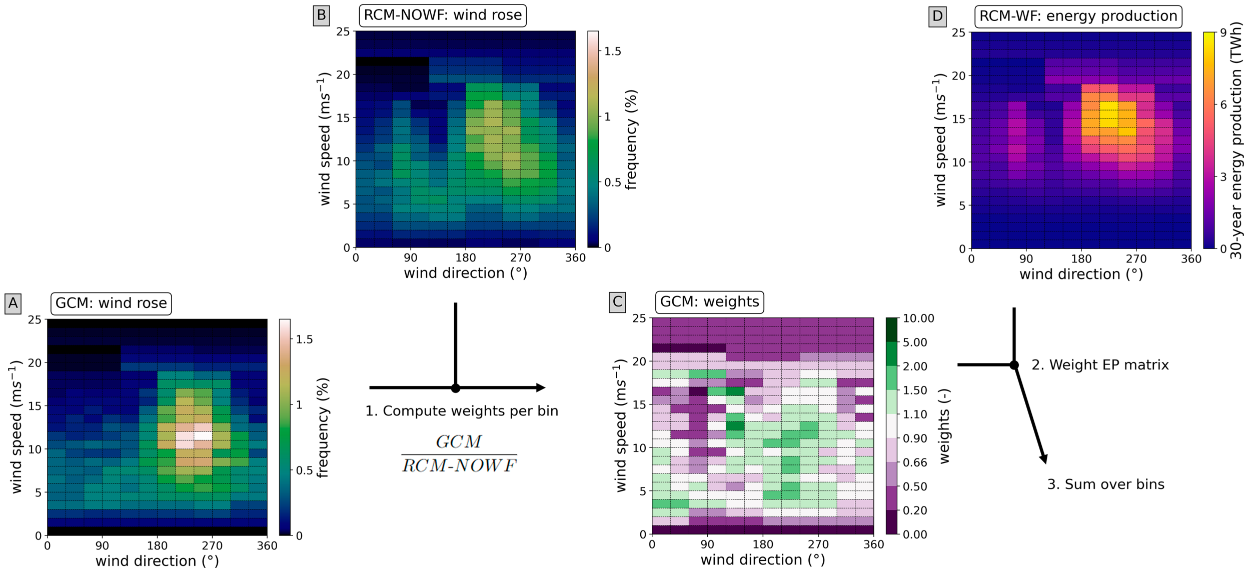

FIG. 2. Graphical flowchart of the statistical–dynamical downscaling algorithm. (a) A 30-yr GCM wind rose at the weighting location. (b) The RCM-NOWF wind rose (after spatial averaging) at the weighting location. (c) The weighting matrix containing frequency ratios between the GCM and RCM per bin. (d) The cumulative EP matrix calculated from the wind farm grid cells in the RCM-WF simulation. An additional text-based flowchart is available in Fig. S4.

RCM simulations with a grid spacing that allows the use of a wind farm parameterization, i.e., below 5 km (Fischereit et al. 2022a). The simulation length should capture the long-term wind climate and output the wind field at a high temporal frequency (e.g., 1 h). In the first simulation (RCM-NOWF), no wind farms are parameterized as they represent the background wind climate at the location of interest, i.e., the region around one or several wind farms. The second simulation (RCM-WF) only differs from RCM-NOWF in that a wind farm parameterization is included so that wind farm–atmosphere interactions, including wake effects, are taken into account. An important requirement for the algorithm is a strong correlation between the two simulations away from the relaxation boundaries in terms of the synoptic-scale winds. The complete algorithm is outlined in Fig. 2. First, the GCM wind rose is constructed at the location of interest (Fig. 2a). Next, the GCM-scale winds are derived from the RCM-NOWF simulation, by averaging over a 110×110 km^2 region centered at the location of interest. After this averaging, the RCM-NOWF wind rose is constructed (Fig. 2b). For each hourly wind field of the RCM-NOWF simulation, the total EP can be deduced from the RCM-WF simulation by integrating the EP over all wind farm grid cells. Hence, each time slice of the RCM simulation is assigned to a wind rose bin and has an EP value associated with it. These EP values can then be summed into a cumulative EP matrix which is binned in the same way as the wind rose (Fig. 2d). Subsequently, the normalized GCM and RCM wind roses are divided to produce a frequency weighting matrix (Fig. 2c), which is used to weight the cumulative EP matrix through elementwise multiplication. Summation over the bins of the weighted energy matrix then provides an estimate of the EP under the wind climate represented by the GCM wind rose. The algorithm is additionally described in a text-based flowchart in Fig. S4. By applying the algorithm for both the historical and future wind roses of a GCM, the difference in EP between the two periods can be estimated for the selected wind farms. Next to the changes in the large-scale wind climate, the algorithm incorporates the effects of mesoscale processes and intra- and interfarm wake effects. Furthermore, interactions between the wind climate changes and wake effects are included, such as the link between changes in the wind direction distribution and interfarm wakes.

In the application presented here, the RCM-NOWF and RCM-WF simulations were performed with COSMO-CLM and are abbreviated as CCLM-NOWF and CCLM-WF, respectively. To capture the full wind climate, the simulations covered 30 years and output was written every hour, so that more than 260 000 values were available per grid cell. Hence, for each wind rose bin, a very large number of instantaneous samples were available so that the underlying variability of the atmospheric profiles was included. The persistence of correlation between CCLM-NOWF and CCLM-WF away from the boundaries was checked for a 100×100 km^2 box centered at a point away from wind farms (56°N, 2.5°E). For the space-averaged wind components, a Pearson correlation coefficient of >0.999 was found, together with a negligible difference in the long-term mean wind speed of $<0.1\%$. Prior to the application of the algorithm, the wind speed data of the GCM simulations were bias corrected to the long-term ERA5 distribution using a quantile mapping approach (e.g., Li et al. 2019). The weighting algorithm and the bias correction were applied separately for each season, i.e., for December–February (DJF), March–May (MAM), June–August (JJA), and September–November (SON), because the North Sea wind climate is highly season dependent. All wind roses were constructed for 100 m above mean sea level (MSL). Some parts of the RCM

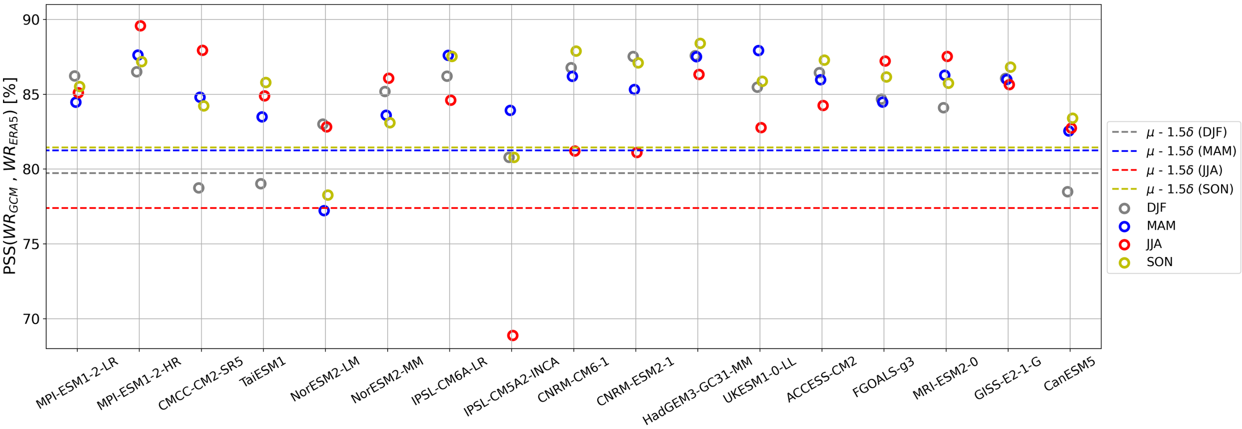

FIG. 3. Performance analysis of the historical GCM simulations based on a comparison with ERA5 for the period 1985–2014, for the winds at 100 m MSL at a central point in the North Sea (55°N, 3°E). Performance is quantified as the overlap between the wind roses, using the PSS. The bin widths are 1 m s^{-1} for wind speed and 20° for wind direction. Models are grouped per model family (Table 1). The dashed lines indicate the cutoff thresholds used for the exclusion of some models.

wind rose were more sparsely populated, typically at low and high wind speeds. Therefore, to avoid empty or very sparse bins, an adaptive binning was used, where the amount of directional bins was reduced according to the amount of data available in the COSMO-CLM simulation for a certain wind speed range. In the first step, the wind rose was constructed with bins of 1 m s^{-1} by 30° above 5 m s^{-1}. Below 5 m s^{-1}, the wind direction bin resolution was reduced to 60°. For each wind speed bin above 5 m s^{-1}, it was checked if there were at least 10 samples per wind rose bin. If not, the number of directional bins was halved down to a minimum of three bins. For very high wind speeds (well above the rated wind speed), no directional subdivision was employed due to very low data counts. This adaptive binning was also done per season.

Applying the weighting algorithm in the center of the North Sea to analyze the impact on the entire wind farm distribution at once is not possible due to the degradation of spatial autocorrelation away from the weighting point. Therefore, the weighting algorithm was applied at eight different points over the North Sea, where each of these points has a collection of wind farms linked to it that are closest to that point (Fig. 1). This approach ensured that each large-scale wind field extracted from the RCM was representative for all the considered wind farms. A few wind farms (~4%) were farther than 100 km from any of the eight points and were not considered in the analysis.

The weighting algorithm relies on the regional model simulation to provide information at the farm scale and to include mesoscale processes and wake effects. To quantify the added value of the RCM involvement, the EP of the wind farms was also estimated directly from the bias-corrected GCM simulations. More specifically, the time series of wind speed were constructed at the hub height of the turbines in each wind farm grid cell through interpolation from the model levels. Next, the wind speed was converted to EP using Eq. (2) and the capacity density in that grid cell. This simplified method does not consider mesoscale processes or wake effects in the estimates of EP but only the changes in the large-scale wind speed distribution. It should be noted that this is still an improvement compared to the common approach where surface wind speeds are extrapolated to hub height using constant extrapolation coefficients as this can introduce large biases (Hahmann et al. 2022).

3. Results

a. GCM analysis

The long-term, seasonal wind roses modeled by the GCMs for the historical period typically match well with their counterparts in the ERA5 reanalysis (Fig. 3). The ensemble does not exhibit consistency in terms of which season has better or worse agreement with the reference. Some models have a substantially lower agreement for one or more seasons compared to the other models. Therefore, a hard threshold was implemented to exclude the GCMs for which the agreement for a season was very low, as it points to insufficient skill in representing the relevant processes that determine the wind rose. Model exclusion based on a performance assessment is one of the common approaches to constraining multimodel ensembles (MMEs) which is based on the assumption that historical performance is a predictor for the quality of future projections (Brunner et al. 2020). For each season, the chosen threshold was the mean minus 1.5x the standard deviation of the PSS values. Hence, five models were excluded from further analyses. The associated wind speed bias for the most problematic season of these models was typically large, with the exception of CanESM5 (Fig. S5). The large wind speed biases for NorESM2-LM (MAM) and CMCC-CM2-SR5 (DJF) are in line with the study of Hahmann et al. (2022), where a similar analysis was done closer to the Danish shore. Their study also showed that this comparison is relatively insensitive to the choice of reanalysis dataset.

The change in the mean wind speed between the future and historical GCM simulations does not exhibit a correlation with the intensity of the radiative forcing of the different SSP scenarios (Fig. S6). This is the case for all seasons. The pattern of

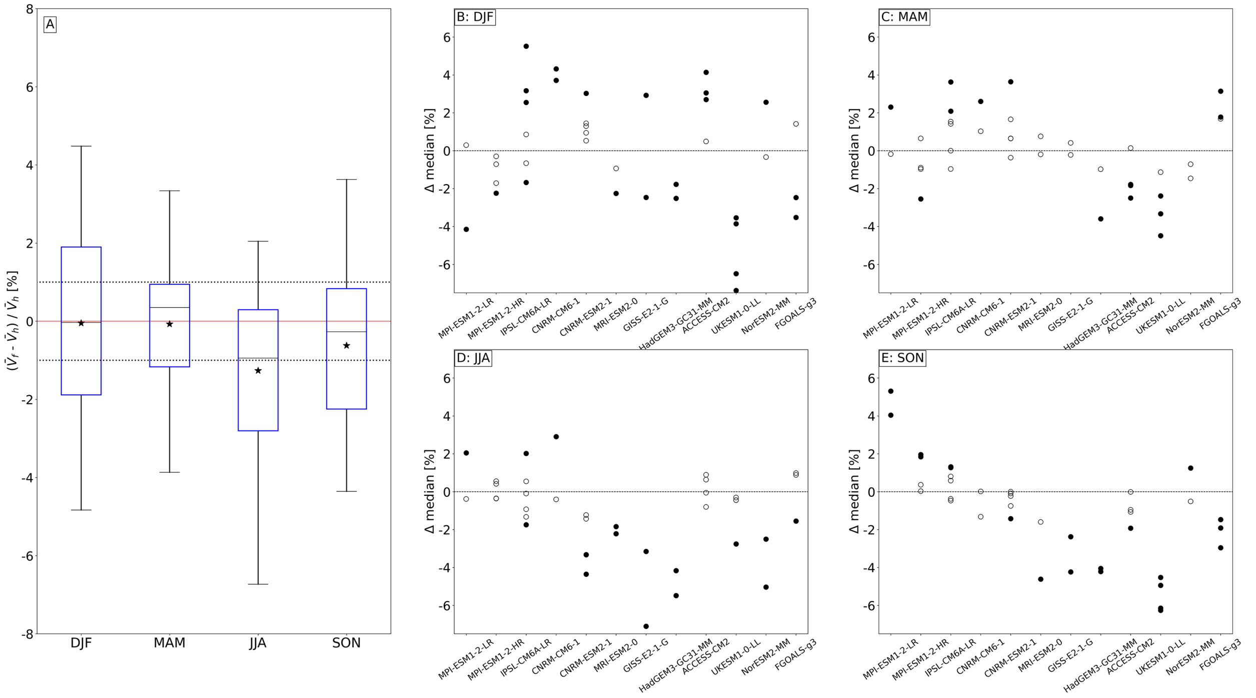

FIG. 4. Ensemble differences in the seasonal wind speed statistics at 10 m between the future (2025–54) and historical (1985–2014) periods of the GCMs. (a) Ensemble distributions of the difference in 30-yr mean wind speed. Boxes are Q25–Q50–Q75, and the whiskers are Q10 and Q90. Asterisks represent the ensemble mean. The dashed, horizontal lines indicate −1% and 1%. (b)–(e) Relative difference in the median wind speed between the future and historical periods for the individual simulations of each GCM. Hollow markers are not significant according to Mood's median test ($\alpha = 0.05$).

which the SSP scenario gives the highest and lowest values is not consistent across the four models. This is not unexpected, as for the considered time window all considered SSPs are quite close to each other in terms of the climate change signal, and so the statistics are dominated by climate variability. Therefore, further analyses will not distinguish among the different SSP scenarios.

The ensemble mean of the 38 CMIP6 simulations for the future period indicates a slight reduction in the mean wind speed for JJA and SON compared to the historical period (Fig. 4a). However, the ensemble spread is large, and for several simulations, an increase can be noted. Hahmann et al. (2022) also found reductions for JJA over this period, albeit stronger. However, their study considered a different simulation ensemble and looked at the period 2031–50. For DJF and MAM, the ensemble mean is very close to zero, but the former has a much larger ensemble spread. The median wind speed changes for DJF are significant for 24 out of the 38 future GCM simulations according to Mood's median test ($\alpha = 0.05$) but are equally distributed between increases and decreases (Fig. 4b). For JJA (SON), 14 (14) out of the 38 simulations have a significant decrease in the median, and 3 (7) simulations have a significant increase. For HadGEM3-GC31-MM and UKESM1-0-LL, reductions seem to be present for all seasons, whereas for most models, the sign of the signal is not the same for all seasons. In general, models with the same atmospheric component do not necessarily exhibit similar signals. The average change between the wind direction distributions of the two 30-yr periods is around 5% for each season (Fig. S7). The strongest change is found for MAM, for which most simulations show fewer easterlies and more westerlies than in the historical period.

We also conducted an analysis of possible future changes in the frequency of wind speeds above the cut-out wind speed (25 $\mathrm{m\ s^{-1}}$), above which wind turbines are stalled (Fig. S8). This indicates that the frequency of storm-force winds over the wind farm lifetime can deviate substantially from the historical baseline, with several GCM projections showing a large increase in the relative frequency from 0.15% (13 $\mathrm{h\ yr^{-1}}$) to 0.24% (21 $\mathrm{h\ yr^{-1}}$). Yet, we recognize that our analysis is limited by the use of data which only represents synoptic-scale winds and has a low temporal resolution (6 h). Therefore, we recommend this topic be investigated in more detail based on high-resolution data products, also because these analyses may have important implications for wind farm operation and maintenance.

b. *Energy production derived from COSMO-CLM*

The 30-yr mean background wind speed of the COSMO-CLM simulations has a range of ~1 $\mathrm{m\ s^{-1}}$ over the eight wind farm groups, for all seasons (Table 3). This spatial variation in wind resources results in differing efficiencies among wind farm groups, reflected in the capacity factor—the ratio of actual energy production to the theoretical maximum energy production (as if the wind farms were constantly operating at full capacity). However, groups with similar mean wind speeds can still have substantially different capacity factors, which can be explained by varying degrees of wake losses, which are themselves determined by the capacity densities of

TABLE 3. Mean background wind speed at 100 m, EP, and capacity factor over the simulation period (1991–2020), for the wind farm groups assigned to the eight different points (see Fig. 1). The 30-yr mean background wind speed is derived from CCLM-NOWF, whereas the 30-yr capacity factor and EP are derived from CCLM-WF.

	$\overline{V}_{100}$ (m s^{-1})				Capacity factor (%)				Energy production (TWh)			
Point	DJF	MAM	JJA	SON	DJF	MAM	JJA	SON	DJF	MAM	JJA	SON
P1	10.8	8.7	7.6	9.3	53.3	37.1	28.7	43.6	63	45	35	52
P2	10.9	8.9	7.8	9.5	49.3	32.7	25.3	40.8	419	283	219	350
P3	11.2	9.1	7.7	9.9	52.6	35.7	25.7	45.1	789	545	392	681
P4	11.5	9.4	7.9	10.1	57.6	42.6	30.7	50.8	351	264	190	312
P5	11.5	9.4	8.0	10.2	52.6	34.5	26.0	45.8	938	626	473	824
P6	11.8	9.6	8.0	10.4	62.9	50.2	38.1	58.0	212	173	131	197
P7	11.9	9.8	8.6	10.8	65.0	51.1	42.2	60.3	189	151	125	177
P8	11.3	9.3	7.9	10.0	61.7	48.7	37.6	55.2	118	94	73	106

the wind farms and the degree of clustering of the wind farms (see Table 2). For example, the wind farms assigned to P2 have high capacity densities and are more tightly clustered than P1, which leads to lower capacity factors.

c. *Application of the weighting algorithm*

An important aspect of the presented weighting method is that it accounts for changes in the wind direction distribution and the effect on wakes in and between wind farms. To illustrate this, a weighted mean wind speed was calculated for CCLM-WF, for both the historical simulation and a future simulation of two GCMs at point P2 (Fig. 5). This weighted mean wind speed was constructed by weighting each hourly wind field with the weighting factor of the wind rose bin that this hour was assigned to. The wake deficits as modeled by the CCLM-WF simulation are clearly visible in and around the wind farms. For UKESM1-0-LL (top), the future JJA period is characterized by lower wind speeds and more

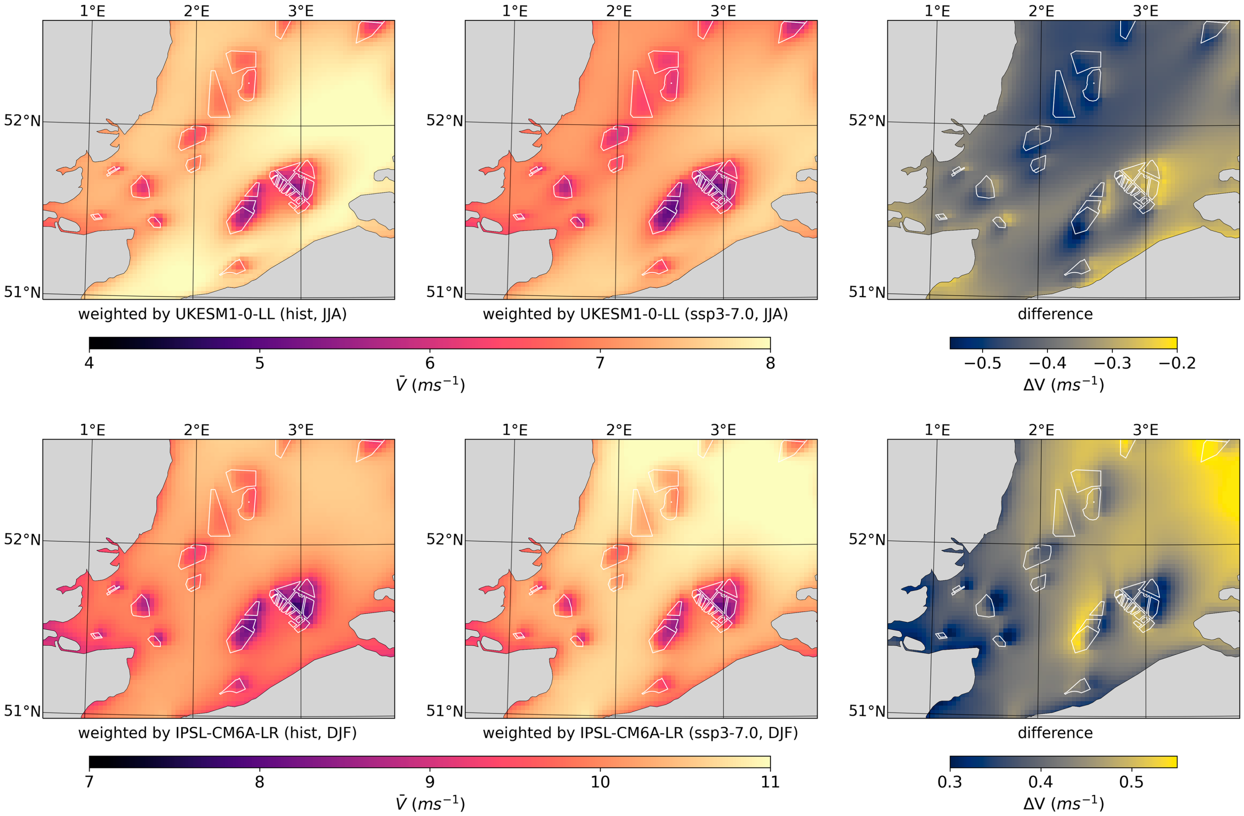

FIG. 5. Weighted mean wind speed at point P2 for the historical simulation (1985–2014) and a future (2025–54) simulation of two GCMs. (top) JJA for UKESM1-0-LL and (bottom) DJF for IPSL-CM6A-LR. White contours represent the outlines of the wind farms in CCLM-WF. The weighted mean wind speed was constructed by weighting each hourly wind field with the weighting factor of the wind rose bin that this hour was assigned to.

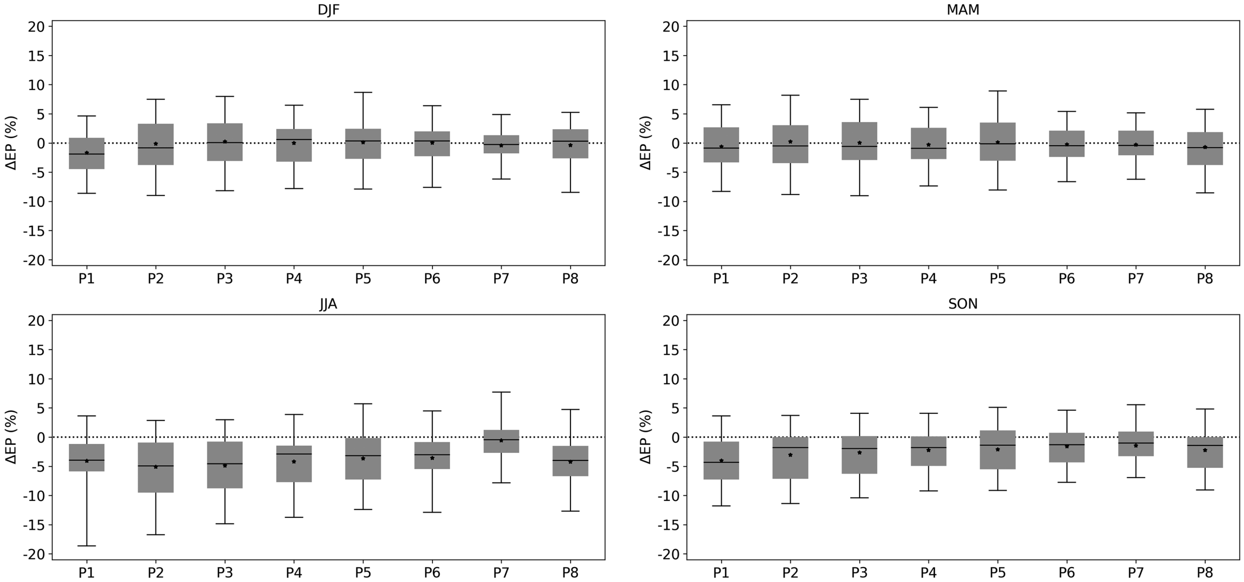

FIG. 6. Ensemble distributions of the difference in the weighted, 30-yr EP between the future (2025–54) and historical (1985–2014) GCM simulations. The EP of each wind farm group is derived after applying the weighting algorithm at the corresponding point (P1–P8). Each boxplot represents the full ensemble of 38 future GCM simulations. Boxes are Q25–Q50–Q75, and the whiskers are minimum and maximum. Asterisks represent the ensemble mean.

northeasterly winds than in the historical period (see Fig. S9). The reduced, large-scale wind speed is clearly captured by the weighting, but so is the impact of the more frequent northeasterly winds: For most wind farms, the strongest reductions can be found on the southwestern side of the wind farm because those grid cells are more frequently waked in the future period than in the historical period. In contrast, the northeastern side of the wind farms is characterized by smaller reductions, as these regions experience fewer wakes. For IPSL-CM6A-LR (bottom), the future DJF simulation is characterized by a higher wind speed and more westerlies (see Fig. S9). After the weighting, the future mean wind speed is higher at all locations, but the increase is considerably weaker on the eastern side of the wind farms, as these regions are waked more under the future wind climate. The effect on interfarm interactions is thus particularly clear.

The differences in the weighted, 30-yr EP between the future and historical GCM simulations are summarized in the form of boxplots for each of the wind farm groups (Fig. 6). Qualitatively, the findings are in agreement with the analysis of the 10-m wind speed changes (see Fig. 6). For DJF and MAM, the ensemble mean is very close to zero, whereas a reduction can be observed for JJA and SON, for most of the wind farm groups. However, in quantitative terms, both the ensemble spread for all seasons and the ensemble mean for JJA and SON are much larger in magnitude. This is the cumulative effect of two mechanisms: First, the relationship between wind speed and the EP of a wind turbine is highly nonlinear (see, e.g., Figs. S1 and S2), so changes in wind speed and EP are not proportional. Second, changes in the wind speed and wind direction distributions can alter the impact of wakes. For wind speed, this effect is linked to the shape of the power curve. Additionally, for both wind speed and wind direction, this is linked to the shape of individual farms (intrafarm wakes) and the positioning of wind farms with respect to one another (interfarm wakes). For the wind farm groups characterized by lower mean wind speeds for JJA and SON, the reductions are stronger on average and the boxplots stretch to larger reductions. These lower mean wind speeds correspond to more of the wind speeds coinciding with the steep section of the power curve, in which small wind speed reductions lead to strong changes in EP. In particular, the wind farms at P7 exhibit remarkably low sensitivity, which follows from the high wind resource there and relatively low sensitivity to wake losses (see Table 2). Because the amount of considered simulations varies over the GCMs, it was required to check if the ensemble mean is largely determined by one or several models with many simulations. To this end, the changes of the 30-yr EP were averaged over the different simulations of each GCM, reducing the amount of data points to 1 per GCM (see Fig. S10). Analysis of the resulting boxplots shows that the negative ensemble mean difference for JJA and SON persists and the ensemble spread is reduced.

As the weighting algorithm can also be applied for GCM wind roses of shorter periods, it was applied for all of the GCM decades from the historical and future periods using a sliding window over the 30-yr periods (Fig. 7). Note that the changes were restricted to the GCM wind rose, whereas the weighting still used the full 30-yr datasets from CCLM-NOWF and CCLM-WF. The EP was summed over all wind farms, after applying the weighting algorithm at the eight different points. The differences between the future and historical distributions can be largely explained by the changes in the median wind speed between the 30-yr periods (Fig. 4).

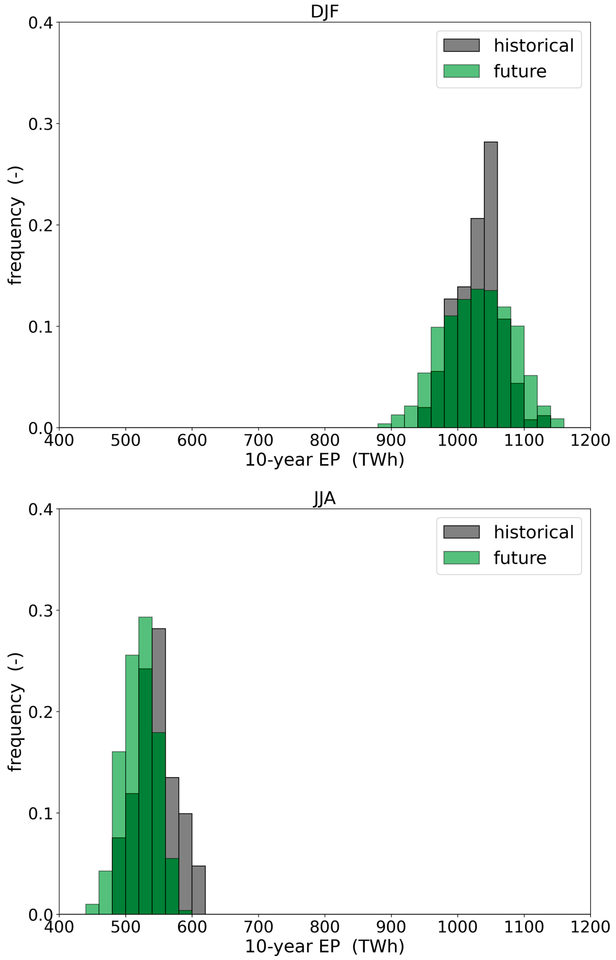

FIG. 7. Normalized histograms of 10-yr, weighted EP for all decades in the future (2025–54) and historical (1985–2014) periods. The EP values are integrated over all wind farm groups, after applying the weighting at each of the eight points (P1–P8). The histograms for the historical (future) periods contain data from all of the corresponding 12 (38) simulations.

For JJA and SON, most GCMs show a reduction in the median wind speed, leading to a higher frequency of low production decades, with some decades even outside of the historical range. For DJF, the median changes translate to fewer average decades and more low and high production decades. The fraction of future decades below specific quantiles of the historical period distribution is summarized in Table 4. The differences between the future and historical periods for DJF, JJA, and SON are similar across the different wind farm groups, with the exception of P7 (see Figs. S11–S18). At P7, the differences for DJF and JJA are relatively small but are still present for SON.

A similar synthesis for single-year GCM wind roses is shown in Fig. 8. The range around the mean annual EP (AEP) is around ±40%, which is much larger than on the 10-yr time scale, where it is around ±10%. The future distributions for JJA and SON have a higher frequency of low production years than in the historical period, but the AEP values are constrained to the historical range. For DJF, the future period has more years of low and high production but also remains well within the historical range. This implies that the increased frequency of low production decades for DJF, JJA, and SON is not a consequence of an increase and intensification of extremely low production years. The disagreement between the future and historical distributions is also much smaller than on the decadal time scale, due to the interannual variability being much larger than the interdecadal variability: The large

TABLE 4. Fraction of the future 10-yr EP values below different percentiles of the EP values from the historical simulations. EP values are integrated over all North Sea wind farms, after applying the weighting algorithm at the eight individual points. These values are based on the complete set of historical and future simulations pooled together.

Season	$<\mathrm{P5}_h$	$<\mathrm{P25}_h$	$<\mathrm{P50}_h$	$<\mathrm{P75}_h$	$<\mathrm{P95}_h$ (%)
DJF	16.2	33.8	54	64.9	87.8
MAM	5.4	27.6	53.9	75.8	94.6
JJA	14.1	52.9	79.9	95.9	100
SON	17.3	49.2	71.4	85.3	95.4

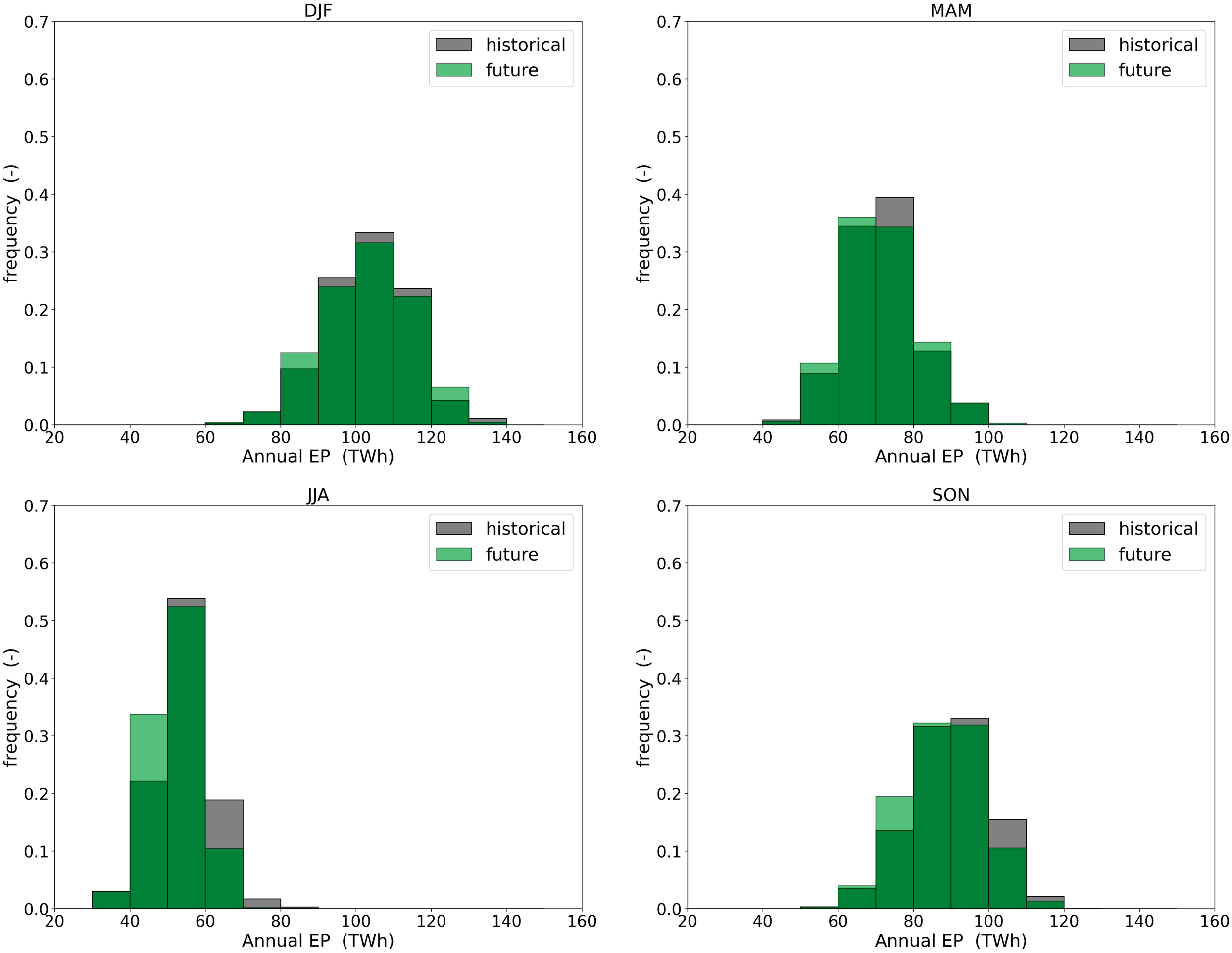

FIG. 8. Normalized histograms of 1-yr, weighted EP for all years in the future (2025–54) and historical (1985–2014) periods. The EP values are integrated over all wind farm groups, after applying the weighting at each of the eight points (P1–P8). The histograms for the historical (future) periods contain data from all of the corresponding 12 (38) simulations.

interannual variability produces a wide AEP distribution in which the (comparatively small) effect of the 30-yr changes (see Fig. 6) is less visible.

The change in 30-yr EP directly estimated from the GCM data agrees quite well with the change derived after applying the weighting algorithm (Fig. 9). This indicates that changes in wake losses due to changes in the wind rose are secondary to the changes in the wind speed distribution, which was also found by Hahmann et al. (2022). However, differences can still reach around 5%, which represents a substantial difference over 30 years. In general, the weighting method leads to stronger changes due to the interaction between the wind climate and wake losses: The EP becomes more (less) sensitive to wakes when the wind speed distribution is shifted to lower (higher) wind speeds due to the interaction with the power curve. Also, changes in the wind direction distribution can increase or decrease wake losses. It is likely that the difference between the two methods can be much larger for shorter time scales, e.g., between two consecutive decades, because the wind rose difference can be larger and so also the increase or decrease in wake losses. Also, the differences might be larger when considering wind farm distributions at later time horizons (e.g., 2050) as interfarm interactions will become more important. Note that the direct estimation method severely overestimates the capacity factors due to the omission of wake effects (see Fig. S19), making it unfit for wind farm efficiency estimation.

4. Discussion

Although the presented weighting approach has similarities with existing statistical–dynamical downscaling methods, it has specific advantages for the estimation of future wind energy production. The wind rose binning uses a high amount of classes (>150), with a finer binning in densely populated parts of the wind rose. For wind speed, a small bin width of 1 m s^{-1} is used, to accommodate the nonlinear relationship with turbine power production. Furthermore, the seasonal wind roses hold on average more than 200 RCM samples per bin, with higher counts for more populated bins, which ensures that the

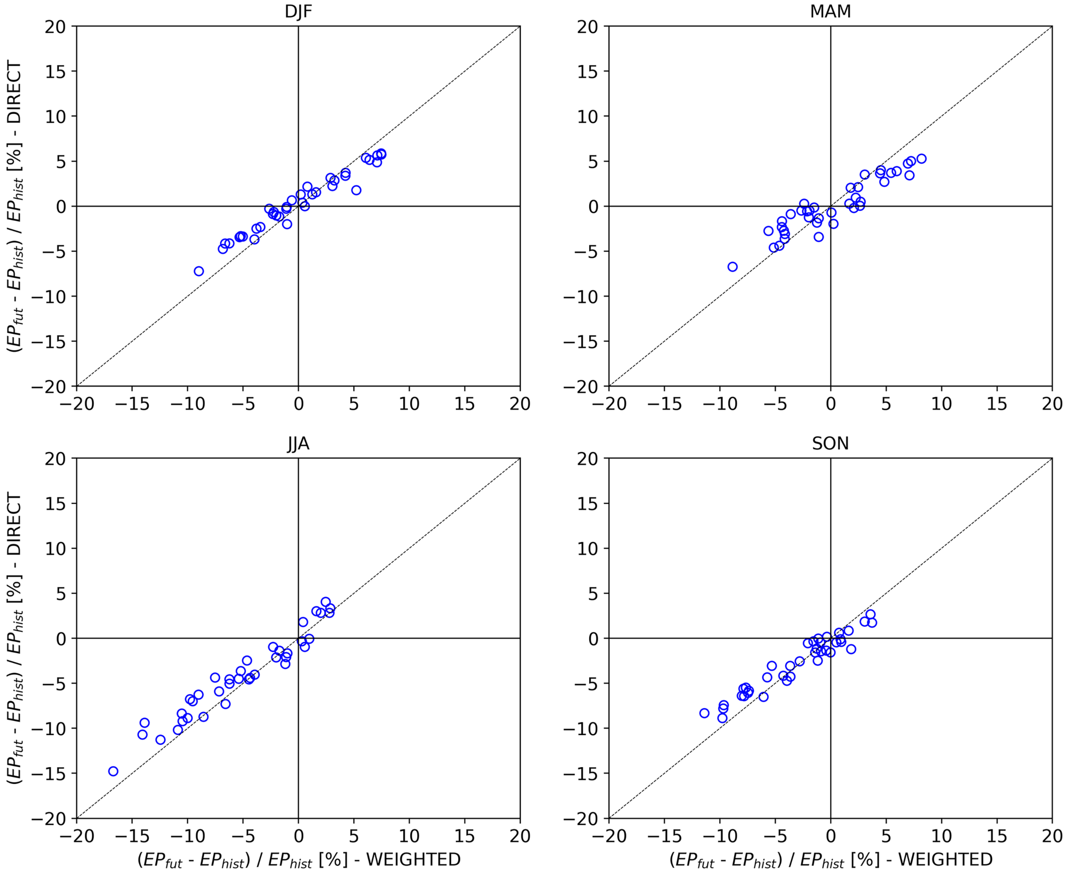

FIG. 9. Scatterplot comparing the relative change in 30-yr EP derived from the weighting method with the one derived from the direct estimation method for all of the future GCM simulations. The change is for the future period (2025–54) relative to the historical period (1985–2014) for the wind farm group around SP2.

underlying atmospheric variability is accounted for. Additionally, by applying the weighting directly at the wind turbine level, errors due to imperfect vertical correlation are avoided compared to the use of, e.g., 850-hPa winds (e.g., Najac et al. 2011). Moreover, both GCM and RCM winds are derived by interpolation from model levels, which avoids errors associated with vertical extrapolation as described in Hahmann et al. (2022). To check the relevance of any remaining interpolation error, we compared the ACCESS-CM2 model winds at the seventh model level (129 m) with interpolated values based on the sixth (76 m) and eighth (195 m) model levels. For wind speed (direction), we find a root-mean-square error (RMSE) of 1.3% (0.6°) and an average of −0.4% (0.3°) which remains constant throughout the years. The mentioned error magnitudes are negligible compared to the wind rose bin widths used in the weighting algorithm, so it has negligible influence on the computation of the weighted EP, more so because the small bias coming from the interpolation error would be present in both the past and future GCM data.

Compared to other statistical–dynamical approaches (e.g., Reyers et al. 2015), this algorithm is more computationally intensive because two continuous, multidecadal climate simulations are required. Yet, these simulations can also be used for other purposes, such as analyses of wake statistics in wind farm clusters or impacts of mesoscale weather systems on power production. It should be noted that this method also has several disadvantages compared to the full dynamical downscaling of a GCM ensemble, e.g., the effect of climatological changes in the stability of the marine PBL is not taken into account. Furthermore, if applied onshore, the method does not take into account the effect of future land-use changes. An additional limitation of the method is that the modeling of wakes and the subsequent calculation of EP are susceptible to the RCM setup and the choice of wind farm parameterization. However, the Fitch wind farm parameterization has been shown to skillfully model wake deficits inside and behind wind farms (Dirksen et al. 2022; Ali et al. 2023) and the long-term EP estimates are relatively insensitive to the amount of TKE added by the parameterization (Rosencrans et al. 2024).

Comparing our findings with previous studies is challenging because most studies considered different model ensembles, time periods, regions, and methodologies. This issue of limited comparability was also pointed out in the review of Jung and Schindler (2022). However, several parallels can be drawn: The near-future reductions in mean EP in JJA of ~5% over the North Sea have also been reported with similar magnitude and ensemble spread by Moemken et al. (2018), Carvalho et al. (2021), and Hahmann et al. (2022). Also, the ensemble average change is reported to be small for the winter season, but again with a large ensemble spread, in line with our findings. The fact that all these studies have worked with different model ensembles increases the confidence in the changes reported by all of these studies. Furthermore, in agreement with our study, studies find negligible differences between SSP scenarios for the near term to midcentury, whereas these differences do appear for end-of-century wind climate projections (e.g., Tobin et al. 2016; Martinez et al. 2023).

As reported by previous studies, the sensitivity of EP to wind climate changes is dependent on the wind turbine characteristics (Moemken et al. 2018; Devis et al. 2018). The tall 15-MW turbines that we assume for most of the future wind farms are relatively robust to wind climate changes due to the low-rated wind speed, above which production is constant, and because they catch stronger winds on average, as was also quantified in Borgers et al. (2024). The use of another turbine model could affect the changes in EP presented here. Whereas most previous work quantifies changes in EP by converting wind speeds to EP via a turbine power curve, we have demonstrated the value of including a realistic wind farm component in the downscaling simulations: First of all, the impacts of wind climate changes on operational and planned installations are more clear. Second, it is not only the characteristics of individual turbines but also turbine density, wind farm shapes, and interfarm distances that determine the change in EP to wind climate changes because these wind farm properties determine the sensitivity of intra- and interfarm wake losses to wind climate changes. Our finding that the impact of wind resource changes can be amplified by the increase or decrease of wake losses in and between wind farms is also in line with the study of Hahmann et al. (2022).

5. Conclusions

In this study, we have introduced a new algorithm for the statistical–dynamical downscaling of GCM projections to quantify future wind energy production. The algorithm combines reanalysis-driven RCM simulations at the kilometer scale with a wind rose weighting to approximate the energy production (EP) of a set of wind farms in the wind climate of a GCM. The wind rose weighting is applied directly at turbine height and uses a fine bin resolution optimized per season. Furthermore, the method accounts for wind farm–atmosphere interaction effects through the use of a wind farm parameterization in the RCM simulations. We have subsequently applied the downscaling algorithm to a large ensemble of CMIP6 GCM simulations to quantify the EP of a projected, 92-GW wind farm distribution in the North Sea for the 2025–54 period. The RCM simulations were performed with COSMO-CLM over a period of 30 years using a 2.8-km grid spacing. An initial set of 17 GCMs was reduced to 12 based on a performance assessment, after which the weighting algorithm was applied to the 12 historical simulations and 38 future simulations.

For all seasons, the change in cumulative EP between 2025–54 and 1985–2014 has a large ensemble spread, with an interquartile range (IQR) of ~8% and a total range of ~15%. The ensemble mean is near zero for DJF and MAM, approximately −5% for JJA, and around −2.5% for SON. The 30-yr mean changes over the ensemble also translate into a different probability distribution of decadal EP compared to the historical period. For DJF, 16% of future decades fall below the P5 production of the historical period and 12% exceed the P95. For JJA (SON), the tendency for long-term wind resource reductions leads to 80% (71%) of future 10-yr EP falling below the historical P50 decadal production. Finally, 30-yr EP changes are underestimated when derived directly from the GCM wind speeds instead of with the wind rose weighting method because the former does not account for the changes in wake losses that follow from changes in the long-term wind rose.

The potential changes in 30-yr, seasonal EP presented could translate to a substantial economic impact but do not necessarily jeopardize the energy provision due to the overdesign of large wind farms (Hahmann et al. 2022). However, these results should be considered in combination with the potential, added wake losses due to the construction of nearby wind farms (e.g., Rosencrans et al. 2024; Borgers et al. 2024) and additional effects such as changes in air density, atmospheric stability, and land-use change. On the other hand, strategic deployment and technological improvements such as the adoption of next-generation turbines or the rollout of energy storage systems can likely compensate the potential resource reductions and can build more energy security (Kara and Şahin 2023; Giddings et al. 2024; Borgers et al. 2024). To further constrain the future energy production in a region, it is recommended to also consider the potential of decadal climate predictions, instead of projections (e.g., Marotzke et al. 2016).

The presented method can be applied to constrain the future EP of any wind farm distribution in any region. However, for applications of the method to wind farm distribution projections at later time horizons (e.g., 2050), uncertainties related to wind farm locations and properties are considerably larger and this needs to be accounted for. This can be done by performing additional mesoscale simulations for a range of wind farm configurations, or by employing a fast engineering model driven by the bias-corrected GCM data, which is more cost effective but lacks interaction between the mesoscale flow and the wind farms and is also not ideal for interfarm wake modeling. A further reduction in the computational cost might be possible by simulating, for example, a representative historical decade with the RCM instead of a full 30-yr period, but it should be verified whether this would sufficiently capture the 30-yr statistics. Because the continuous RCM simulations can also be used for other applications, such as more in-depth studies on wakes or temporal variability, they could be embedded in wider research projects. Also, the multidecadal COSMO-CLM simulations performed for this work are made publicly available to the community.

Acknowledgments. This research has been supported by the project FREEWIND, funded by the Energy Transition Fund of the Belgian Federal Public Service for Economy, SMEs, and Energy (FOD Economie, K.M.O., Middenstand en

Energie). The computational resources and services in this work were provided by the VSC (Flemish Supercomputer Center), funded by the Research Foundation Flanders (FWO) and the Flemish Government Department EWI. JGP thanks the AXA Research Fund for support.

Data availability statement. The COSMO-CLM simulation output used in this study is made available through a GLOBUS interface that can be accessed via the website of the FREEWIND project at https://freewind-project.eu/. In addition to the simulations presented here, there are several other simulation products available there, including a simulation with a present-day wind farm distribution and several simulations with a projected 2050 wind farm distribution. Furthermore, the wind farm distribution used in this study and the interpolated CMIP6 wind speeds and wind directions over the North Sea (at 100 m MSL) are made public to the community through Zenodo (Borgers 2024b). Finally, the updated wind farm parameterization code developed in the context of this study is also made available through Zenodo, accompanied by a step-by-step implementation guide for COSMO5-CLM15 (Borgers 2024a).

REFERENCES

Akhtar, N., and F. Chatterjee, 2020: Wind farm parametrization in cosmo5.0_clm15. World Data Center for Climate (WDCC) at DKRZ, accessed 1 November 2020, https://doi.org/10.35089/WDCC/WindFarmPCOSMO5.0clm15.

——, B. Geyer, B. Rockel, P. S. Sommer, and C. Schrum, 2021: Accelerating deployment of offshore wind energy alter wind climate and reduce future power generation potentials. *Sci. Rep.*, **11**, 11826, https://doi.org/10.1038/s41598-021-91283-3.

Ali, K., D. M. Schultz, A. Revell, T. Stallard, and P. Ouro, 2023: Assessment of five wind-farm parameterizations in the Weather Research and Forecasting Model: A case study of wind farms in the North Sea. *Mon. Wea. Rev.*, **151**, 2333–2359, https://doi.org/10.1175/MWR-D-23-0006.1.

Bak, C., and Coauthors, 2013: The DTU 10-MW reference wind turbine. DTU Orbit, accessed 6 May 2022, https://orbit.dtu.dk/en/publications/the-dtu-10-mw-reference-wind-turbine.

Bento, N., and M. Fontes, 2019: Emergence of floating offshore wind energy: Technology and industry. *Renewable Sustainable Energy Rev.*, **99**, 66–82, https://doi.org/10.1016/j.rser.2018.09.035.

Bi, D., and Coauthors, 2020: Configuration and spin-up of ACCESS-CM2, the new generation Australian Community Climate and Earth System Simulator Coupled Model. *J. South. Hemisphere Earth Syst. Sci.*, **70**, 225–251, https://doi.org/10.1071/ES19040.

Bodini, N., J. K. Lundquist, D. Zardi, and M. Handschy, 2016: Year-to-year correlation, record length, and overconfidence in wind resource assessment. *Wind Energy Sci.*, **1**, 115–128, https://doi.org/10.5194/wes-1-115-2016.

Borgers, R., 2024a: Fitch wind farm parametrization in COSMO5-CLM15 - V3. Zenodo, accessed 26 June 2024, https://doi.org/10.5281/zenodo.12547570.

——, 2024b: ResearchData_FutureResourceUncertainty_GCMs_and_windfarms. Zenodo, accessed 26 June 2024, https://doi.org/10.5281/zenodo.12549096.

——, and Coauthors, 2024: Mesoscale modelling of North Sea wind resources with COSMO-CLM: Model evaluation and impact assessment of future wind farm characteristics on cluster-scale wake losses. *Wind Energy Sci.*, **9**, 697–719, https://doi.org/10.5194/wes-9-697-2024.

Boucher, O., and Coauthors, 2020: Presentation and evaluation of the IPSL-CM6A-LR climate model. *J. Adv. Model. Earth Syst.*, **12**, e2019MS002010, https://doi.org/10.1029/2019MS002010.

Brisson, E., M. Demuzere, and N. P. M. van Lipzig, 2016: Modelling strategies for performing convection-permitting climate simulations. *Meteor. Z.*, **25**, 149–163, https://doi.org/10.1127/metz/2015/0598.

Brunner, L., and Coauthors, 2020: Comparing methods to constrain future European climate projections using a consistent framework. *J. Climate*, **33**, 8671–8692, https://doi.org/10.1175/JCLI-D-19-0953.1.

Carta, J. A., S. Velázquez, and P. Cabrera, 2013: A review of Measure-Correlate-Predict (MCP) methods used to estimate long-term wind characteristics at a target site. *Renewable Sustainable Energy Rev.*, **27**, 362–400, https://doi.org/10.1016/j.rser.2013.07.004.

Carvalho, D., A. Rocha, X. Costoya, M. deCastro, and M. Gómez-Gesteira, 2021: Wind energy resource over Europe under CMIP6 future climate projections: What changes from CMIP5 to CMIP6. *Renewable Sustainable Energy Rev.*, **151**, 111594, https://doi.org/10.1016/j.rser.2021.111594.

Chatterjee, F., D. Allaerts, U. Blahak, J. Meyers, and N. P. M. van Lipzig, 2016: Evaluation of a wind-farm parametrization in a regional climate model using large eddy simulations. *Quart. J. Roy. Meteor. Soc.*, **142**, 3152–3161, https://doi.org/10.1002/qj.2896.

Cherchi, A., and Coauthors, 2019: Global mean climate and main patterns of variability in the CMCC-CM2 coupled model. *J. Adv. Model. Earth Syst.*, **11**, 185–209, https://doi.org/10.1029/2018MS001369.

Devis, A., N. P. M. Van Lipzig, and M. Demuzere, 2018: Should future wind speed changes be taken into account in wind farm development? *Environ. Res. Lett.*, **13**, 064012, https://doi.org/10.1088/1748-9326/aabff7.

Dirksen, M., I. Wijnant, P. Siebesma, P. Baas, and N. E. Theeuwes, 2022: Validation of wind farm parameterisation in weather forecast model HARMONIE-AROME: Analysis of 2019. Delft University of Technology Internal Rep. WP5 and WP6, 68 pp., https://www.wins50.nl/downloads/dirksen_etal_validationreport.pdf.

Doms, G., and M. Baldauf, 2013: A description of the nonhydrostatic regional COSMO-Model. Part I: Dynamics and numerics. COSMO Tech. Rep. 5, 166 pp., https://doi.org/10.5676/DWD_pub/nwv/cosmo-doc_5.00_I.

——, and Coauthors, 2013: A description of the nonhydrostatic regional COSMO-Model. Part II: Physical parametrization. COSMO Tech. Rep. 5, 162 pp., https://doi.org/10.5676/DWD_pub/nwv/cosmo-doc_5.00_II.

EMODnet, 2023: Wind farms (polygons). EMODnet Human Activities, accessed 30 January 2023, https://emodnet.ec.europa.eu/en/human-activities#humanactivities-data-products.

European Commission, 2020: Communication from the commission to the European parliament, the council, the European economic and social committee and the committee of the regions. European Union, accessed 13 May 2024, https://eur-lex.europa.eu/legal-content/EN/TXT/?uri=COM:2020:741:FIN&qid=1605792629666.

Eyring, V., S. Bony, G. A. Meehl, C. A. Senior, B. Stevens, R. J. Stouffer, and K. E. Taylor, 2016: Overview of the Coupled Model Intercomparison Project Phase 6 (CMIP6) experimental design and organization. *Geosci. Model Dev.*, **9**, 1937–1958, https://doi.org/10.5194/gmd-9-1937-2016.

Fant, C., C. Adam Schlosser, and K. Strzepek, 2016: The impact of climate change on wind and solar resources in Southern Africa. *Appl. Energy*, **161**, 556–564, https://doi.org/10.1016/j.apenergy.2015.03.042.

Feser, F., M. Barcikowska, O. Krueger, F. Schenk, R. Weisse, and L. Xia, 2015: Storminess over the North Atlantic and northwestern Europe—A review. *Quart. J. Roy. Meteor. Soc.*, **141**, 350–382, https://doi.org/10.1002/qj.2364.

Fischereit, J., R. Brown, X. G. Larsén, J. Badger, and G. Hawkes, 2022a: Review of mesoscale wind-farm parametrizations and their applications. *Bound.-Layer Meteor.*, **182**, 175–224, https://doi.org/10.1007/s10546-021-00652-y.

——, X. G. Larsén, and A. N. Hahmann, 2022b: Climatic impacts of wind-wave-wake interactions in offshore wind farms. *Front. Energy Res.*, **10**, 881459, https://doi.org/10.3389/fenrg.2022.881459.

——, K. Schaldemose Hansen, X. G. Larsén, M. P. van der Laan, P.-E. Réthoré, and J. P. Murcia Leon, 2022c: Comparing and validating intra-farm and farm-to-farm wakes across different mesoscale and high-resolution wake models. *Wind Energy Sci.*, **7**, 1069–1091, https://doi.org/10.5194/wes-7-1069-2022.

Fitch, A. C., J. B. Olson, J. K. Lundquist, J. Dudhia, A. K. Gupta, J. Michalakes, and I. Barstad, 2012: Local and mesoscale impacts of wind farms as parameterized in a mesoscale NWP model. *Mon. Wea. Rev.*, **140**, 3017–3038, https://doi.org/10.1175/MWR-D-11-00352.1.

Gaertner, E., and Coauthors, 2020: IEA wind TCP Task 37: Definition of the IEA 15-megawatt offshore reference wind turbine. NREL Tech. Rep. NREL/TP-5000-75698, 54 pp., https://doi.org/10.2172/1603478.

Garcia-Santiago, O. M., J. Badger, A. N. Hahmann, and G. L. da Costa, 2022: Evaluation of two mesoscale wind farm parametrisations with offshore tall masts. *J. Phys.: Conf. Series*, **2265**, 022038, https://doi.org/10.1088/1742-6596/2265/2/022038.

Giddings, J., H. Bloomfield, R. James, and M. Blair, 2024: The impact of future UK offshore wind farm distribution and climate change on generation performance and variability. *Environ. Res. Lett.*, **19**, 064022, https://doi.org/10.1088/1748-9326/ad489b.

Hahmann, A. N., O. García-Santiago, and A. Peña, 2022: Current and future wind energy resources in the North Sea according to CMIP6. *Wind Energy Sci.*, **7**, 2373–2391, https://doi.org/10.5194/wes-7-2373-2022.

Hersbach, H., and Coauthors, 2020: The ERA5 global reanalysis. *Quart. J. Roy. Meteor. Soc.*, **146**, 1999–2049, https://doi.org/10.1002/qj.3803.

Hueging, H., R. Haas, K. Born, D. Jacob, and J. G. Pinto, 2013: Regional changes in wind energy potential over Europe using regional climate model ensemble projections. *J. Appl. Meteor. Climatol.*, **52**, 903–917, https://doi.org/10.1175/JAMC-D-12-086.1.

International Renewable Energy Agency, 2024: Renewable capacity statistics 2024, International Renewable Energy Agency, Abu Dhabi, accessed 13 May 2024, https://www.irena.org/Publications/2024/Mar/Renewable-capacity-statistics-2024.

Jerez, S., J. M. López-Romero, M. Turco, R. Lorente-Plazas, J. J. Gómez-Navarro, P. Jiménez-Guerrero, and J. P. Montávez, 2020: On the spin-up period in WRF simulations over Europe: Trade-offs between length and seasonality. *J. Adv. Model. Earth Syst.*, **12**, e2019MS001945, https://doi.org/10.1029/2019MS001945.

Jonkman, J., S. Butterfield, W. Musial, and G. Scott, 2009: Definition of a 5-MW reference wind turbine for offshore system development. NREL Tech. Rep. NREL/TP-500-38060, 75 pp., https://doi.org/10.2172/947422.

Jung, C., and D. Schindler, 2022: A review of recent studies on wind resource projections under climate change. *Renewable Sustainable Energy Rev.*, **165**, 112596, https://doi.org/10.1016/j.rser.2022.112596.

Kalverla, P. C., A. A. M. Holtslag, R. J. Ronda, and G.-J. Steeneveld, 2020: Quality of wind characteristics in recent wind atlases over the North Sea. *Quart. J. Roy. Meteor. Soc.*, **146**, 1498–1515, https://doi.org/10.1002/qj.3748.

Kara, T., and A. D. Şahin, 2023: Implications of climate change on wind energy potential. *Sustainability*, **15**, 14822, https://doi.org/10.3390/su152014822.

Karnauskas, K. B., J. K. Lundquist, and L. Zhang, 2018: Southward shift of the global wind energy resource under high carbon dioxide emissions. *Nat. Geosci.*, **11**, 38–43, https://doi.org/10.1038/s41561-017-0029-9.

Kawai, H., S. Yukimoto, T. Koshiro, N. Oshima, T. Tanaka, H. Yoshimura, and R. Nagasawa, 2019: Significant improvement of cloud representation in the global climate model MRI-ESM2. *Geosci. Model Dev.*, **12**, 2875–2897, https://doi.org/10.5194/gmd-12-2875-2019.

Kelley, M., and Coauthors, 2020: GISS-E2.1: Configurations and climatology. *J. Adv. Model. Earth Syst.*, **12**, e2019MS002025, https://doi.org/10.1029/2019MS002025.

Kim, B., K. Lee, K. Ko, and J. Choi, 2022: Offshore wind resource assessment off the coast of Daejeong, Jeju Island using 30-year wind estimates. *Sci. Rep.*, **12**, 14179, https://doi.org/10.1038/s41598-022-18447-7.

Lee, W.-L., and Coauthors, 2020: Taiwan Earth System Model Version 1: Description and evaluation of mean state. *Geosci. Model Dev.*, **13**, 3887–3904, https://doi.org/10.5194/gmd-13-3887-2020.

Li, C., J. M. Mogollón, A. Tukker, J. Dong, D. von Terzi, C. Zhang, and B. Steubing, 2022: Future material requirements for global sustainable offshore wind energy development. *Renewable Sustainable Energy Rev.*, **164**, 112603, https://doi.org/10.1016/j.rser.2022.112603.

Li, D., J. Feng, Z. Xu, B. Yin, H. Shi, and J. Qi, 2019: Statistical bias correction for simulated wind speeds over CORDEX-East Asia. *Earth Space Sci.*, **6**, 200–211, https://doi.org/10.1029/2018EA000493.

Li, L., and Coauthors, 2020: The Flexible Global Ocean-Atmosphere-Land System model grid-point version 3 (FGOALS-g3): Description and evaluation. *J. Adv. Model. Earth Syst.*, **12**, e2019MS002012, https://doi.org/10.1029/2019MS002012.

Marotzke, J., and Coauthors, 2016: MiKlip: A national research project on decadal climate prediction. *Bull. Amer. Meteor. Soc.*, **97**, 2379–2394, https://doi.org/10.1175/BAMS-D-15-00184.1.

Martinez, A., L. Murphy, and G. Iglesias, 2023: Evolution of offshore wind resources in northern Europe under climate change. *Energy*, **269**, 126655, https://doi.org/10.1016/j.energy.2023.126655.

Mauritsen, T., and Coauthors, 2019: Developments in the MPI-M Earth System Model Version 1.2 (MPI-ESM1.2) and its response to increasing CO_2. *J. Adv. Model. Earth Syst.*, **11**, 998–1038, https://doi.org/10.1029/2018MS001400.

Mellor, G. L., and T. Yamada, 1982: Development of a turbulence closure model for geophysical fluid problems. *Rev. Geophys.*, **20**, 851–875, https://doi.org/10.1029/RG020i004p00851.

Mengelkamp, H.-T., 1999: Wind climate simulation over complex terrain and wind turbine energy output estimation. *Theor. Appl. Climatol.*, **63**, 129–139, https://doi.org/10.1007/s007040050098.

Moemken, J., M. Reyers, H. Feldmann, and J. G. Pinto, 2018: Future changes of wind speed and wind energy potentials in EURO-CORDEX ensemble simulations. *J. Geophys. Res. Atmos.*, **123**, 6373–6389, https://doi.org/10.1029/2018JD028473.

Müller, W. A., and Coauthors, 2018: A higher-resolution version of the Max Planck Institute Earth System Model (MPI-ESM1.2-HR). *J. Adv. Model. Earth Syst.*, **10**, 1383–1413, https://doi.org/10.1029/2017MS001217.

Najac, J., C. Lac, and L. Terray, 2011: Impact of climate change on surface winds in France using a statistical-dynamical downscaling method with mesoscale modelling. *Int. J. Climatol.*, **31**, 415–430, https://doi.org/10.1002/joc.2075.

O'Neill, B. C., and Coauthors, 2016: The Scenario Model Intercomparison Project (ScenarioMIP) for CMIP6. *Geosci. Model Dev.*, **9**, 3461–3482, https://doi.org/10.5194/gmd-9-3461-2016.

Olauson, J., 2018: ERA5: The new champion of wind power modelling? *Renewable Energy*, **126**, 322–331, https://doi.org/10.1016/j.renene.2018.03.056.

Ostend Declaration, 2023: Ostend Declaration on the North Sea as Europe's Green Power Plant. Ostend Declaration Doc., 8 pp., https://www.government.nl/documents/diplomatic-statements/2023/04/24/ostend-declaration-on-the-north-sea-as-europes-green-power-plant.

Petrie, R., and Coauthors, 2021: Coordinating an operational data distribution network for CMIP6 data. *Geosci. Model Dev.*, **14**, 629–644, https://doi.org/10.5194/gmd-14-629-2021.

Pryor, S. C., and A. N. Hahmann, 2019: Downscaling wind. Oxford University Press, accessed 15 April 2023, https://doi.org/10.1093/acrefore/9780190228620.013.730.

Reyers, M., J. G. Pinto, and J. Moemken, 2015: Statistical–dynamical downscaling for wind energy potentials: Evaluation and applications to decadal hindcasts and climate change projections. *Int. J. Climatol.*, **35**, 229–244, https://doi.org/10.1002/joc.3975.

Rijkswaterstraat, 2023: Aangewezen windgebieden NWP. Accessed 5 June 2023, https://maps.rijkswaterstaat.nl/dataregister/srv/dut/catalog.search#/metadata/1ddc2091-243f-4457-bc90-429f865ef72c.

Ritter, B., and J.-F. Geleyn, 1992: A comprehensive radiation scheme for numerical weather prediction models with potential applications in climate simulations. *Mon. Wea. Rev.*, **120**, 303–325, https://doi.org/10.1175/1520-0493(1992)120<0303:ACRSFN>2.0.CO;2.

Rockel, B., A. Will, and A. Hense, 2008: The regional climate model COSMO-CLM (CCLM). *Meteor. Z.*, **17**, 347–348, https://doi.org/10.1127/0941-2948/2008/0309.

Rosencrans, D., J. K. Lundquist, M. Optis, A. Rybchuk, N. Bodini, and M. Rossol, 2024: Seasonal variability of wake impacts on us mid-Atlantic offshore wind plant power production. *Wind Energy Sci.*, **9**, 555–583, https://doi.org/10.5194/wes-9-555-2024.

Séférian, R., and Coauthors, 2019: Evaluation of CNRM Earth System Model, CNRM-ESM2-1: Role of Earth system processes in present-day and future climate. *J. Adv. Model. Earth Syst.*, **11**, 4182–4227, https://doi.org/10.1029/2019MS001791.

Seland, Ø., and Coauthors, 2020: Overview of the Norwegian Earth System Model (NorESM2) and key climate response of CMIP6 deck, historical, and scenario simulations. *Geosci. Model Dev.*, **13**, 6165–6200, https://doi.org/10.5194/gmd-13-6165-2020.

Sellar, and Coauthors, 2020: Implementation of U.K. Earth system models for CMIP6. *J. Adv. Model. Earth Syst.*, **12**, e2019MS001946, https://doi.org/10.1029/2019MS001946.

Sempreviva, A. M., R. J. Barthelmie, and S. C. Pryor, 2008: Review of methodologies for offshore wind resource assessment in European seas. *Surv. Geophys.*, **29**, 471–497, https://doi.org/10.1007/s10712-008-9050-2.

Sepulchre, P., and Coauthors, 2020: IPSL-CM5A2—An Earth system model designed for multi-millennial climate simulations. *Geosci. Model Dev.*, **13**, 3011–3053, https://doi.org/10.5194/gmd-13-3011-2020.

Shields, M., P. Beiter, J. Nunemaker, A. Cooperman, and P. Duffy, 2021: Impacts of turbine and plant upsizing on the levelized cost of energy for offshore wind. *Appl. Energy*, **298**, 117189, https://doi.org/10.1016/j.apenergy.2021.117189.

Slavik, K., C. Lemmen, W. Zhang, O. Kerimoglu, K. Klingbeil, and K. W. Wirtz, 2019: The large-scale impact of offshore wind farm structures on pelagic primary productivity in the southern North Sea. *Hydrobiologia*, **845**, 35–53, https://doi.org/10.1007/s10750-018-3653-5.

Soares, P. M. M., D. C. A. Lima, and M. Nogueira, 2020: Global offshore wind energy resources using the new ERA-5 reanalysis. *Environ. Res. Lett.*, **15**, 1040a2, https://doi.org/10.1088/1748-9326/abb10d.

Swart, N. C., and Coauthors, 2019: The Canadian Earth System Model version 5 (CanESM5.0.3). *Geosci. Model Dev.*, **12**, 4823–4873, https://doi.org/10.5194/gmd-12-4823-2019.

The Crown Estate, 2023: Wind Site Agreements (England, Wales & NI), The Crown Estate, accessed 5 June 2023, https://opendata-thecrownestate.opendata.arcgis.com/search?q=wind%20site%20agreements.

Tiedtke, M., 1989: A comprehensive mass flux scheme for cumulus parameterization in large-scale models. *Mon. Wea. Rev.*, **117**, 1779–1800, https://doi.org/10.1175/1520-0493(1989)117%3C1779:ACMFSF%3E2.0.CO;2.

Tobin, I., and Coauthors, 2016: Climate change impacts on the power generation potential of a European mid-century wind farms scenario. *Environ. Res. Lett.*, **11**, 034013, https://doi.org/10.1088/1748-9326/11/3/034013.

van Stratum, B., N. Theeuwes, J. Barkmeijer, B. van Ulft, and I. Wijnant, 2022: A one-year-long evaluation of a wind-farm parameterization in HARMONIE-AROME. *J. Adv. Model. Earth Syst.*, **14**, e2021MS002947, https://doi.org/10.1029/2021MS002947.

Vigin, L., 2022: Shapefiles of the Belgian and Dunkirk offshore zones. Royal Belgian Institute of Natural Sciences, accessed 19 January 2022, https://www.bmdc.be/NODC/index.xhtml.

Voldoire, A., and Coauthors, 2019: Evaluation of CMIP6 DECK experiments with CNRM-CM6-1. *J. Adv. Model. Earth Syst.*, **11**, 2177–2213, https://doi.org/10.1029/2019MS001683.

Volker, P. J. H., A. N. Hahmann, J. Badger, and H. E. Jørgensen, 2017: Prospects for generating electricity by large onshore and offshore wind farms. *Environ. Res. Lett.*, **12**, 034022, https://doi.org/10.1088/1748-9326/aa5d86.

World Meteorological Organization, 2017: WMO Guidelines on the calculation of climate normals. WMO Tech. Rep. 1203, 29 pp., https://library.wmo.int/records/item/55797-wmo-guidelines-on-the-calculation-of-climate-normals?offset=5.

Zekeik, Y., M. J. OrtizBevia, F. J. Alvarez-Garcia, A. Haddi, Y. El Mourabit, and A. RuizdeElvira, 2024: Long-term assessment of Morocco's offshore wind energy potential using ERA5 and IFREMER wind data. *J. Mar. Sci. Eng.*, **12**, 460, https://doi.org/10.3390/jmse12030460.

Zhao, X., G. Huang, C. Lu, Y. Li, and C. Tian, 2024: Assessing climate change impacts on wind energy resources over China based on CMIP6 multimodel ensemble. *Environ. Sci. Technol. Lett.*, **11**, 95–100, https://doi.org/10.1021/acs.estlett.3c00829.